Oxidation of Metals (2021) 96:43–55
https://doi.org/10.1007/s11085-021-10044-9

ORIGINAL PAPER

Performance Comparison Between Isothermal Hot Corrosion And In Situ Cyclic Hot Corrosion of Nickel-Based Superalloys

Adnan. U. Syed[1] · Fabian Duarte Martinez[1] · Tracey Roberts[1] · Adriana Encinas-Oropesa[1] · Nicolau I. Morar[1] · Marlene Grohne[2] · Martin Frommherz[2] · John R. Nicholls[1] · Simon Gray[1]

Received: 29 May 2021 / Revised: 29 May 2021 / Accepted: 30 May 2021 /
Published online: 28 June 2021

Abstract

Although a lot of work has been done to understand both major mechanisms of hot corrosion, namely type I (high-temperature hot corrosion) and type II (low temperature hot corrosion), there is very little information available on more representative cyclic performance in these regimes. This work addresses this by assessing the performance of isothermal (type I and type II) hot corrosion tests against combined (short and long) cyclic corrosion tests. Single-crystal alloy PWA 1484 and directionally solidified alloy MAR-M247 were assessed in all test regimes. Pre- and post-exposure dimensional metrology was used to quantify the corrosion damage and characterised using SEM/EDX. This paper highlights that the results of short cycle test conditions are more damaging compared to long cycle and standard isothermal type I and II test conditions. The cast nickel-based alloy MAR-M247 was found to be a better performer compared to PWA 1484 single-crystal alloy.

Keywords Hot corrosion · Isothermal · Thermal cyclic · MAR-M247 · PWA 1484

Introduction

Hot corrosion (HC) is an aggressive mode of attack typically experienced in the under-platform region of aero-gas turbine blades. It results from the reaction of the fuel with contaminants in the air inlet, which leads to the formation of molten deposits, typically Na_2SO_4 [1]. There are two established temperature-dependent modes of HC. Type I hot corrosion (Type I HC) is mainly observed at temperatures between ~ 800–950 °C, above the melting point of the alkali metal salt, while

✉ Adnan. U. Syed
adnan.syed@cranfield.ac.uk

Extended author information available on the last page of the article

Type II hot corrosion (Type II HC) occurs at temperatures between ~ 600–750 °C and involves the formation of a low temperature eutectic Na_2SO_4-MSO_4 (where M is Ni or Co) [2]. Type II HC is not expected to proceed without the minimum partial pressure of SO_3 required for the formation of low melting eutectics [3]. This may be due to the interaction of Na_2SO_4 with $NiSO_4$ or with other impurities present in the turbine environment (i.e. NaCl). HC tests are being widely conducted in many laboratories across academia and industry using isothermal conditions. However, there is very little information available on thermal cyclic HC performance. During service, gas turbines undergo many thermal cycles and therefore it is important to acquire thermal cyclic HC data [4]. Thermal cycling can be detrimental from a corrosion point of view since the difference in thermal expansion coefficient between the metal and the oxide scale may lead to large compressive stresses in the scale. Consequently, different modes of mechanical failure of the scale can occur, such as buckling, delamination, cracking and in some cases spallation of the oxide, which can have a major effect on the hot corrosion resistance of the alloys [5]. Whether spallation occurs depends on a complex interplay of conditions, such as the maximum operating temperature, the test environment, accumulated time at maximum temperature and heating/cooling rates. For this reason, accounting for these events is of utmost importance to understand the mechanism that underlies the corrosion resistance of nickel-based superalloys. For chromia and alumina forming alloys, spallation events can be a significant problem due to the loss of the scale forming element in the near surface region. Such non-protective attack takes place when the scale-forming elements (Al and Cr) fall below a critical level.

MAR-M247 is a polycrystalline conventionally cast nickel-based superalloy and PWA 1484 is a single-crystal nickel-based superalloy, both considered for turbine blade materials. Unlike polycrystalline alloys, single-crystal superalloys do not contain grain boundary hardening elements, such as Zr, C and B. In addition, the Cr content typically increases within the order: polycrystalline, directionally solidified and single crystal [6]. These changes in composition as well as other microstructural differences between polycrystalline and single-crystal superalloys yield considerable differences in their corrosion behaviour, which needs to be investigated. The current study uses both isothermal and cyclic HC tests to gain an understanding of high-temperature degradation behaviour and influence of alloying additions.

Experimental Procedures

Superalloys MAR-M247 DS and PWA 1484 alloys were used in this study. The nominal composition is given in Table 1. The centreless ground finished material was cut into small cylindrical specimens (length of approximately 10 mm, with diameter approximately 8.5 mm). Before use, the samples were cleaned in an ultrasonic bath for 20 min in (a) acetone followed by (b) isopropyl alcohol (IPA). The dimensions of each sample were measured using a digital micrometer with a resolution of ± 0.001 mm.

The isothermal hot corrosion tests were carried out in vertical controlled atmosphere furnace systems (Fig. 1a). These alumina lined furnaces are designed to

Table 1 Alloy composition used in corrosion tests

Material	Nominal composition (weight %)												
	Ni	Co	Cr	Al	Ta	W	Mo	Re	Ti	Hf	B	Zr	C
PWA 1484	Bal	10.0	5.0	5.6	6.5	8.7	5.9	3.0	–	0.1	–	–	–
MAR-M247	Bal	10.0	8.4	5.5	3.0	10.0	0.7	–	1.0	1.5	0.015	0.05	0.15

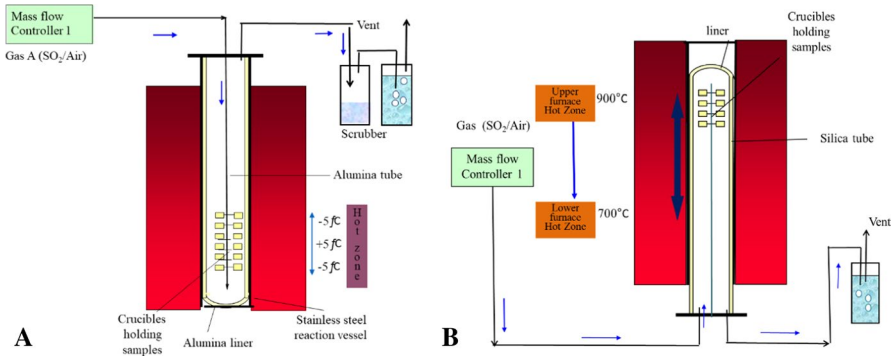

Fig. 1 Schematic diagram of a vertical controlled atmosphere furnace set-up for **a** isothermal and **b** thermal cyclic hot corrosion test in simulated root pocket area for IP turbines [7]

accommodate 24 alumina crucibles (containing the samples) that sit in an alumina frame. The thermal cyclic tests were carried out in a cyclic rig designed at Cranfield University UK, which can accommodate 16 specimens placed in crucibles that sit in the frame and enclosed with glass tube (Fig. 1b). The thermal cyclic rig cycles between two zones at different temperatures.

A schematic of the test cycles used in this work is shown in Fig. 2. Figure 2a represents the standard isothermal hot corrosion test used which does not simulate thermal strains placed on the material in service. Figure 2b represents a short cycle that was designed to simulate short 'island-hoping' flights, and finally, Fig. 2C shows the long cycle designed to represent longer 'cruise-type' flights. The heating and cooling rate of the isothermal test was controlled to 6 °C min^{-1}. However, the rates in the cyclic tests are not controlled since the furnaces are already at temperature when the rig is cycled which again is more representative to engine conditions. The number of cycles was selected so all three profiles had a total hot exposure time of 40 h before being removed for inspection and resalting (explained later).

A deposit salt solution of 80%Na_2SO_4-20%K_2SO_4 (mol%) at a flux of 5 µg/cm^2/h was sprayed onto each specimen prior to exposure. During this, samples were kept on the hot plate at approximately 180 °C to ensure flash evaporation of the water in the solution.

Table 2 lists the test matrix for samples exposed to isothermal and thermal cyclic test conditions. Isothermal testing was designed to run for 520 h, with each inspection cycle of 40 h. Short cyclic test with a cycle length of 2.5 h was designed to run

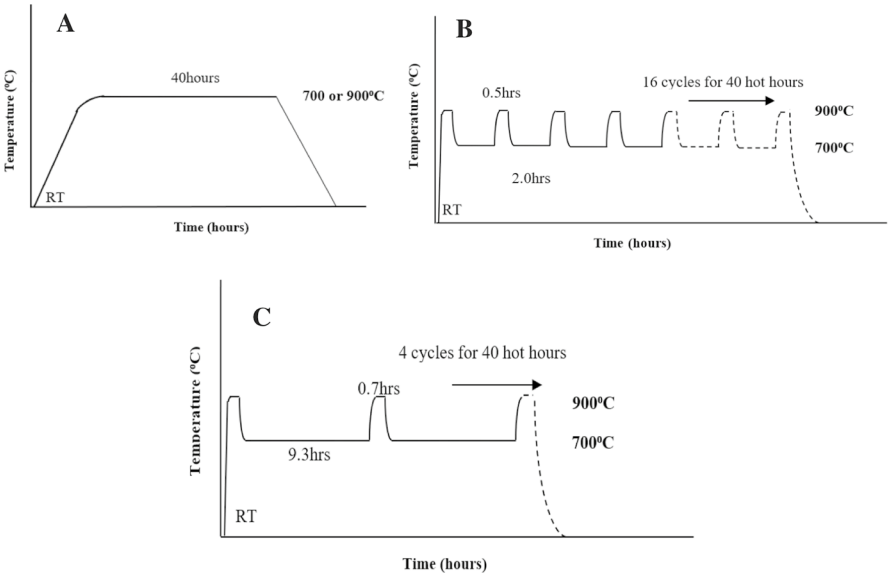

Fig. 2 Schematic representation of thermal cycle for each 40-h resalting/inspection period for **a** isothermal, **b** short cycle and **c** long cycle tests

for 640 h (256 cycles), and long cyclic test with a cycle length of 10 h was run for 560 h (56 cycles). After every 40-h inspection cycle, the samples were unloaded from the furnace and weighed then redeposited with the same salt deposit compositions, weighed again and loaded back into the furnace for another 40-h inspection cycle. After the final exposure, samples were weighed, before being examined. The surfaces of selected samples were examined using scanning electron microscopy (SEM) and energy-dispersive X-ray (EDX) analysis to determine the morphology and chemical composition. Polished cross sections were prepared through the midpoint of all the samples using and established metallographic procedure [8]. These cross sections were all measured using an image analyser to generate accurate measurements of the remaining amount of metal after the corrosion tests; these measurements were compared to the pre-exposure metal dimensions to produce distributions of metal loss due to corrosion which is required for the development of hot corrosion damage models.

Results and Discussion

SEM/EDX Analysis

Figure 3 shows the scales formed on alloy MAR-M247 are thicker compared to those formed on alloy PWA 1484 in the LC test. Both alloys were exposed for the same time of 560 h. The total thickness of the scale (outer oxide scale + internal oxide/sulphide layer) formed on alloy MAR-M247 is almost 1.8 times larger

Table 2 Test conditions for isothermal and cyclic hot corrosion testing

Test No	Temperature (°C)	Exposure time (h)	Total number of cycles	Deposit (mol%)	Alloys type
1	900 (Type I)	520	NA	80%Na_2SO_4-20%K_2SO_4	Alloy MAR-M247 &Alloy PWA 1484
2	700 (Type II)	520	NA		
3	900–700 (Short cycle)	640	256		
4	900–700 (Long cycle)	560	56		

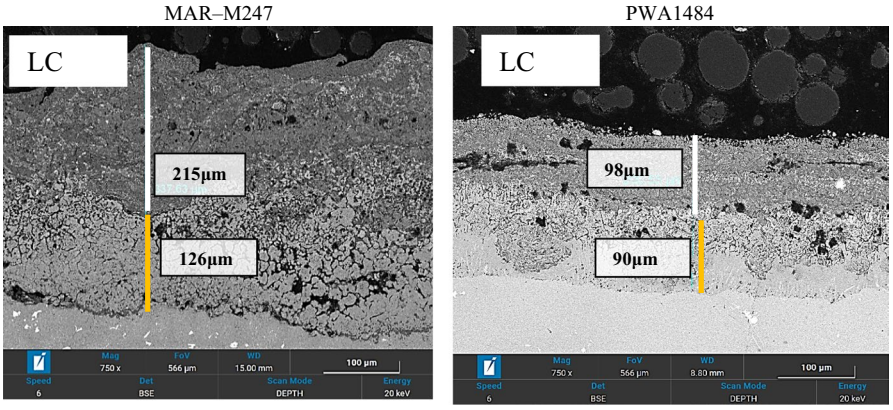

Fig. 3 Backscattered images of cross sections through alloy MAR-M247 and PWA 1484 samples covered with deposits (80%Na_2SO_4-20%K_2SO_4) exposed to air + 300 vppm SOx gaseous atmosphere gas within long cyclic test conditions for 560 h between 700–900 °C

(~ 341 microns) than on the lower chromium PWA 1484 (~ 188 microns). Figure 3 also indicates that the thick scale formed on MAR-M247 is coherent and well adhered to the surface, whereas the scale formed on PWA 1484 shows lateral crack formation near the scale/gas interface and multiples voids within the outer and internal oxide layers. Another interesting feature is the rough oxide scale formed on MAR-M247, which was not found in the scale for alloy PWA 1484, where the scale surface was found to be smoother. It could be argued that the thick scale form on MAR-M247 is due to the presence of grain boundaries, which enhances the metal diffusion process. However, the difference in alloy composition may also be playing a role. The scale on PWA 1484 exhibits distinctive layers consisting of chromia at the gas/scale interface, alumina at the scale/metal interface, and a rutile-type structures as $CrTaO_4$ in between, as evidenced by the EDX maps in Fig. 8. This $CrTaO_4$, which is known to inhibit metal diffusion [9, 10], may form in this alloy due to the higher concentration of Ta.

Figure 4 shows that when the alloys are exposed to the same (short cycle) test conditions, MAR-M247 again forms thicker scales (outer oxide scale + internal oxide/sulphide layer) compared to alloy PWA 1484. It is shown that the total scale thickness (~ 509 microns) formed on alloy MAR-M247 is almost 3 times the thickness of the scale formed on alloy PWA 1484. Another interesting feature is that the internal oxide formed on PWA 1484 alloy in SC conditions is very similar in its morphology and thickness to the internal oxide formed in the LC test conditions.

The outward growing oxides on MAR-M247 were found to be thicker and illustrate significant presence of voids and pores in comparison with the outer oxide formed on PWA 1484. Such performance difference is likely to be due to the presence of grain boundaries, which can act as fast diffusion path.

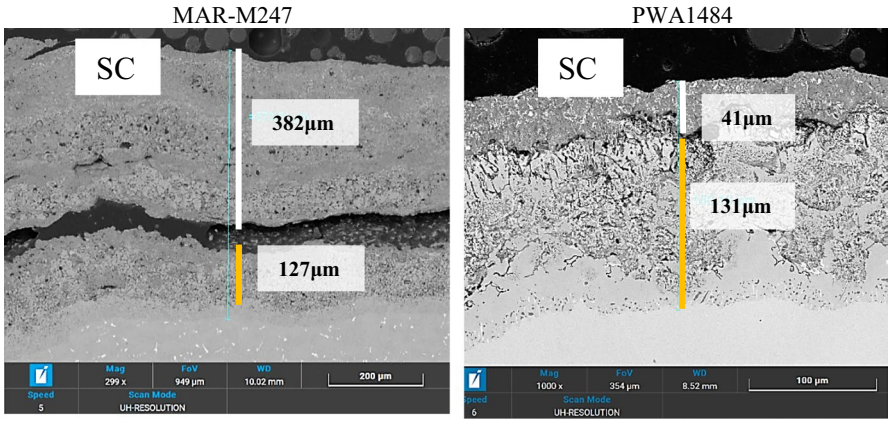

Fig. 4 Backscattered images of cross sections through alloy MAR-M247 and PWA 1484 samples covered with deposits ($80\%Na_2SO_4$-$20\%K_2SO_4$) exposed to air + 300 vppm SOx gaseous atmosphere gas within SC test conditions for 640 h between 700–900 °C

Comparison of Long and Short Cycle Tests

Figure 5 shows the cross-sectional images of MAR-M247 exposed to SC and LC tests conditions for 640 and 560 h, respectively. The images show that the hot corrosion depth in the SC test condition was approximately double in comparison with the LC test condition. It is also noticeable that the internal metal oxide layer formed in both test conditions is significantly thinner compared to the outer oxide scale. An important feature observed is the scale de-cohesion at the metal/scale interface in both test conditions. The scale detachment at the metal/scale interface indicates a weak mix metal oxide/sulphide scales formation for both alloys. Such test conditions

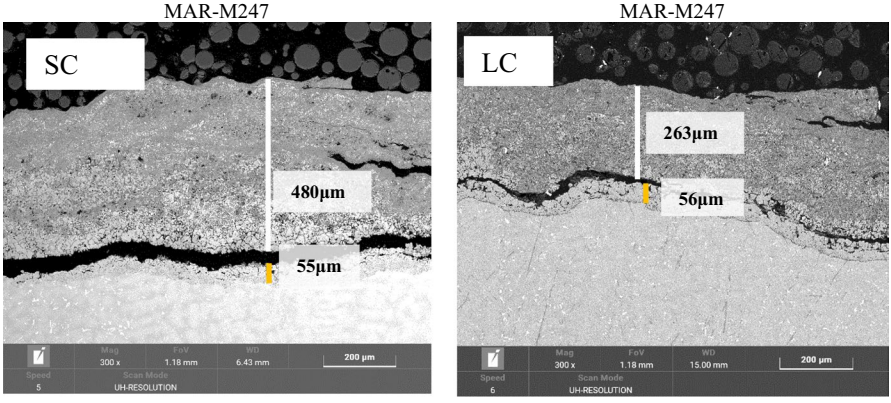

Fig. 5 Backscattered images of cross sections through alloy MAR-M247 samples covered with deposits ($80\%Na_2SO_4$-$20\%K_2SO_4$) exposed to air + 300 vppm SOx gaseous atmosphere gas within SC test for 640 and LC test conditions for 560 h between 700–900 °C

simulate long and short term flights and suggest that short distance flights are more detrimental for the jet engines service schedule.

Thermal Cycle and Isothermal Tests Comparison

Figure 6 shows BSE images of polished cross section of PWA 1484 exposed to thermal cyclic (SC & LC) and isothermal (Type I and Type II) test conditions. It is clear that the sample exposed to Type I conditions formed much thicker scales compared to samples exposed to Type II and thermal cyclic tests. The distinctive features observed for Type I HC image appear to follow the well-established basic fluxing mechanism that is dissociation of Na_2SO_4 into Na_2O and SO_3 and its reaction with Cr_2O_3 to form chromate and sulphide. The expected pitting type attack for Type II HC is not evident within the cross-sectional image for Type II test conditions; instead, the attach was broad front. This is likely due to the corrosion attack progressing well into the propagation stage, where the pits are merged to form a thick uniform scale. The total scale thickness for LC and SC is approximately ~ 200

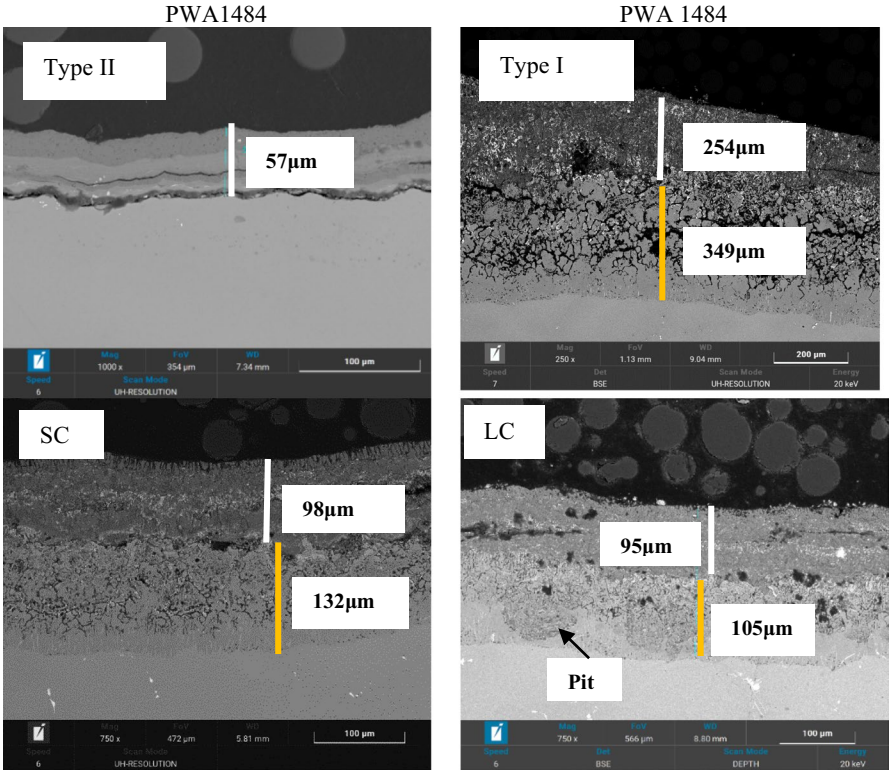

Fig. 6 Backscattered images of cross sections through alloy PWA 1484 samples covered with deposits (80%Na_2SO_4-20%K_2SO_4) exposed to air + 300 vppm SOx gaseous atmosphere gas within SC test for 640 and LC test conditions for 560 h between 700–900 °C and isothermal Type I and Type II for 520 h at 900 and 700 °C, respectively

microns; however, the morphological appearance of the scales is very different. Two distinctive layers are exhibited in both LC and SC images, where the internal scales at metal/scale interface are likely to be a mix of metal sulphides and metal oxides (chromia and alumina) and external scales are resultant oxides of nickel and cobalt. The internal oxidation zone is thicker in the SC test compared to LC test. An interesting feature noticed in the LC image is the formation of wave-shape pits within the internal scale, which was absent in the SC image. Samples exposed to 700 °C for a longer period showed the formation of pits within the internal scale, which highlights characteristic features of type II HC attack.

EDX Mapping

Figure 7 shows EDX mapping of MAR-M247 exposed to LC test conditions for 560 h. It is clearly shown that oxygen is distributed throughout the scale. Ni is richer towards the outer scale/gas interface and metal/internal oxide interface. High level of S was detected close to the metal/internal oxide interface possibly as NiS. Significant patches of Co are present towards the scale/gas interface, and Ti is also evident at the middle and the top region of the outer oxide layer. The inner oxide zone has significant porosity where the Al and Ti presence is richer compared to a region within the scale where Ni and Co are concentrated at the outer oxide layer/

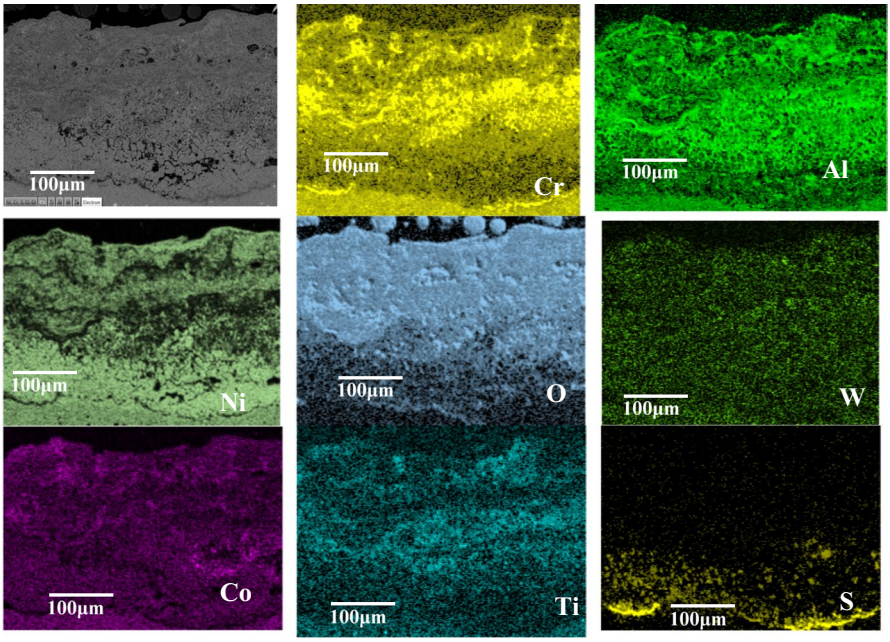

Fig. 7 BSE image and EDX maps of cross sections through alloy MAR-M247 samples covered with (80%Na_2SO_4-20%K_2SO_4) deposit exposed to air + 300 vppm SOx gaseous atmosphere gas within LC test conditions for 560 h between 700–900 °C

gas interface. The significant presence of Cr, Al, S and O suggests presence of their sulphides and oxides.

Figure 8 illustrates EDX mapping of a cross section through alloy PWA 1484 after 560-h testing under LC. These maps show the distribution of oxygen throughout the scale (outer scale and internal oxide/sulphide zone). Significant presence of Al was found with in the inner oxidation and sulphidation zone. EDX maps also shows the rich presence of Ni and S within the inner oxide/sulphide layer suggesting NiS formation. An interesting feature found is the significant presence of Ta across the scale which is in line with previous work [11], suggesting the claim that refractory elements addition in single-crystal low chromium alloys activates sulphide formation (e.g. Re/Ta sulphides) that aids resistance to hot corrosion by inhibiting NiS_x formation. However, the significant presence of S indicates internal sulphidation attack localised at metal/inner oxide/sulphide interface.

Dimensional Metrology

The dimensional metrology results provide the best measurements of the corrosion rate of the different alloy materials [12, 13]. The output provides a distribution of metal damage data for each sample exposed. Figure 9 illustrates the effect of exposure to thermal cyclic and isothermal HC test conditions of both alloys in

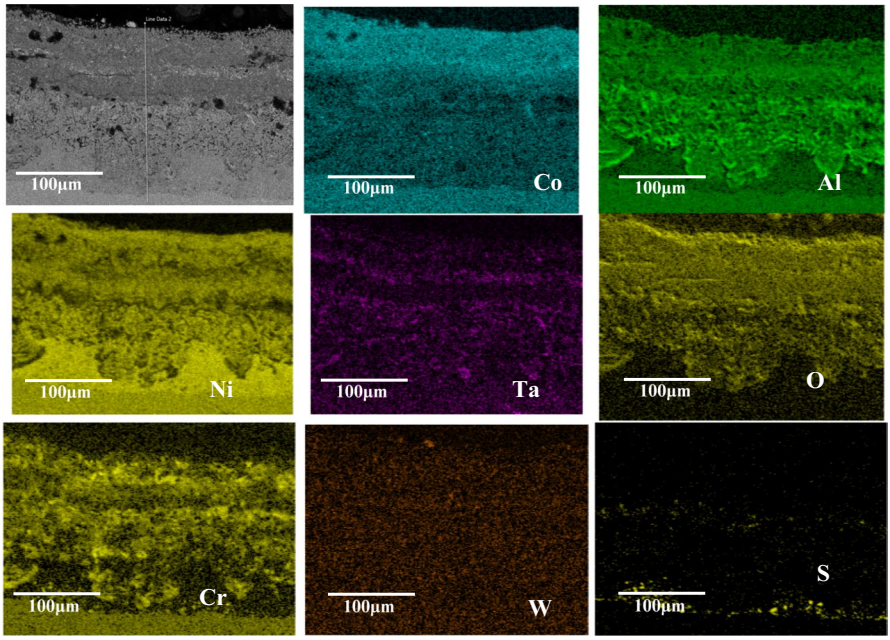

Fig. 8 BSE image and EDX maps of cross sections through alloy PWA 1484 samples covered with ($80\%Na_2SO_4$-$20\%K_2SO_4$) deposit exposed to air + 300 vppm SOx gaseous atmosphere gas within LC test conditions for 560 h between 700–900 °C

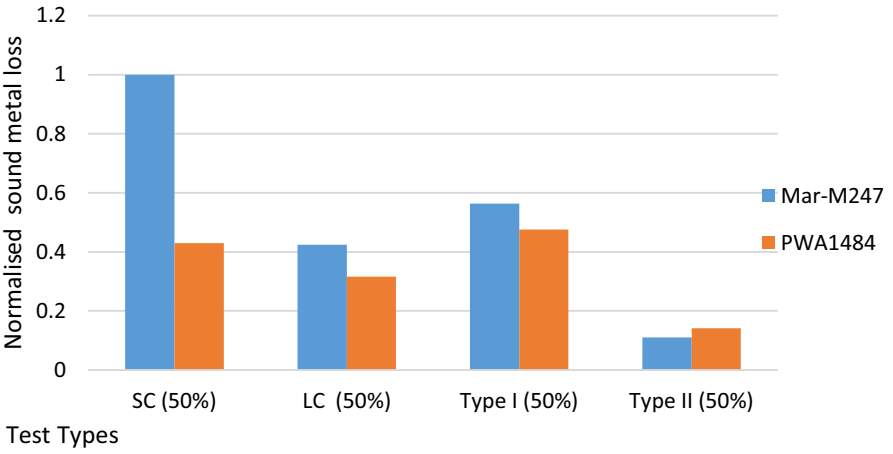

Fig. 9 Comparison of the median metal losses of the alloys PWA 1484 and MAR-M247 after exposure to simulated (thermal cyclic and isothermal) test conditions

terms of 'metal loss'. Normalized median (50%) metal loss values in Fig. 9 shows that MAR-M247 exhibits the most severe corrosion damage. As previously mentioned, one of the factors which makes MAR-M247 a poorer performer is due to it being a directionally solidified material, which contains grain boundaries, versus single-crystal PWA 1484 alloy.

High metal loss values for MAR-M247 are also in line with scale thickness data. It is also to be noted that such behaviour was more significant for MAR-M247 compared to PWA 1484 where the magnitude of difference is almost double. Both alloys exposed to isothermal Type I HC conditions showed high metal loss values compared to metal loss values found for samples exposed to Type II HC conditions which is also in line with scale thickness values observed in BSE images. These datasets show that the relative performance of the alloys can be ranked (in the order from high to low corrosion damage) as SC > Type I > LC > Type II. The results suggest that SC test conditions that simulate conditions for jet engines used for short distance flights exhibit higher corrosion rate compared to results observed for LC test conditions simulating long distance flights.

Conclusions

The study of cyclic HC testing in addition to isothermal testing is important for a better simulation of jet engine turbine components performance. This paper reports the results of hot corrosion isothermal exposures carried out at 700 and 900 °C and thermal cyclic SC and LC tests using the well-established deposit recoat test method. The alloy performances were evaluated using SEM/EDX techniques and dimensional metrology.

- The corrosion damage produced by short cyclic test was significantly higher than long cyclic test conditions.
- Both alloys show two distinctive scales.
  - Significant presence of Al- and Cr-rich oxides layers,
  - Outer damage via formation of noticeable Ni/Co oxides,
  - Refractory elements signal in EDX maps as strengthening role.
- MAR-M247 was found to suffer a higher degree of corrosion in 3 test conditions (LC, SC and Type I HC) by showing high metal loss and thick scales.
- The overall corrosion rate for all four systems was found to be in the order SC > Type I > LC > Type II. However, for PWA 1484 the corrosion rate under Type I and SC conditions is almost similar.

Acknowledgements Funding was provided by German Federal Ministry of Economics and MTU Aero Engines AG (Grant number 20T1522A).

References

1. X. Ma and H.-J. Shi, On the fatigue small crack behaviors of directionally solidified superalloy DZ4 by in situ SEM observations. *International Journal of Fatigue* **35**, (1), 2012 (91–98).
2. R. A. Rapp, Hot corrosion of materials: a¯fluxing mechanism? *Corrosion Science* **44**, 2002 (201–221).
3. P. Lortrakul, R. W. Trice, K. P. Trumble, and M. A. Dayananda, "Investigation of the mechanisms of Type-II hot corrosion of superalloy CMSX-4," *Corrosion Science*, 2014.
4. M. Göbel, A. Rahmel, and M. Schütze, The cyclic-oxidation behavior of several nickel-base single-crystal superalloys without and with coatings. *Oxidation of Metals* **41**, (3–4), 1994 (271–300).
5. E. N'dah, M. P. Hierro, K. Borrero, and F. J. Pérez, Study of the cyclic oxidation resistance of superalloy IN-625: Lifetime predicted by COSP-modelling program. *Oxidation of Metals* **68**, (1–2), 2007 (9–21).
6. S. Wee, et al., Review on mechanical thermal properties of superalloys and thermal barrier coating used in gas turbines. *Applied Sciences (Switzerland)* **10**, (16), 2020 (5476).
7. A. Syed, *Fireside corrosion study of superheater materials in advanced power plants*, (Cranfield University, Cranfield, 2011).
8. N. J. Simms, J. E. Oakey, and J. R. Nicholls, "Development and application of a methodology for the measurement of corrosion and erosion damage in laboratory, burner rig and plant environments," *Materials at High Temperatures*, 2000.
9. W. Ren, et al., The influence of CrTaO4 layer on the oxidation behavior of a directionally-solidified nickel-based superalloy at 850–900 °C. *Journal of Alloys Compound* **724**, 2017 (565–574).
10. J. A. Nychka, D. R. Clarke, and G. H. Meier, "Spallation and transient oxide growth on PWA 1484 superalloy," *Materials Science and Engineering A*, (2008).

11. J. X. Chang, D. Wang, G. Zhang, L. H. Lou, and J. Zhang, "Effect of Re and Ta on hot corrosion resistance of nickel-base single crystal superalloys," in *Proceedings of the International Symposium on Superalloys*, 2016.
12. A. U. Syed, N. J. Simms, and J. E. Oakey, Fireside corrosion of superheaters: Effects of air and oxy-firing of coal and biomass. *Fuel* **101**, 2012 (62–73).
13. T. Hussain, A. U. Syed, and N. J. Simms, Fireside corrosion of superheater materials in coal/biomass co-fired advanced power plants. *Oxidation of Metals* **80**, (5–6), 2013 (529–540).

Authors and Affiliations

Adnan. U. Syed[1] · Fabian Duarte Martinez[1] · Tracey Roberts[1] · Adriana Encinas-Oropesa[1] · Nicolau I. Morar[1] · Marlene Grohne[2] · Martin Frommherz[2] · John R. Nicholls[1] · Simon Gray[1]

Fabian Duarte Martinez
Fabian.Duarte-Martinez@cranfield.ac.uk

Tracey Roberts
T.Roberts@cranfield.ac.uk

Adriana Encinas-Oropesa
A.Encinas-Oropesa@cranfield.ac.uk

Nicolau I. Morar
n.i.morar@cranfield.ac.uk

Marlene Grohne
Marlene.grohne@mtu.de

Martin Frommherz
Martin.frommherz@mtu.de

John R. Nicholls
J.R.Nicholls@cranfield.ac.uk

Simon Gray
s.gray@cranfield.ac.uk

[1] Surface Engineering and Precision Centre, Cranfield University, Bedford MK43 0AL, UK

[2] MTU Aero Engines AG, Dachauer Str. 665, 80995 Munich, Germany